Amide-functionalized carbon supports for cobalt oxide toward oxygen reduction reaction in Zn-air battery

Jing Liu [a,b], Luhua Jiang [a,*], Qiwen Tang [a], Erdong Wang [a], Luting Qi [a], Suli Wang [a], Gongquan Sun [a,*]

[a] Division of Fuel Cell & Battery, Dalian National Laboratory for Clean Energy, Dalian Institute of Chemical Physics, Chinese Academy of Sciences, Dalian 116023, China
[b] University of Chinese Academy of Sciences, Beijing 10049, China

ARTICLE INFO

ABSTRACT

N-doped carbon materials are extensively reported active toward the oxygen reduction reaction (ORR). Different from N-doped carbon, in this study, we report a kind of non-doped nitrogen, i.e., amide-groups, over carbon surface promoting the ORR activity of a CoO_x/C—N composite. The amide-groups are successfully grafted over carbon surface (C—N) via a simple solvothermal route demonstrated by Fourier transform infrared spectra (FTIR) and X-ray photoelectron spectroscope (XPS). After loaded cobalt oxide nanoparticles of around 2 nm in average, the amide-group grafting carbon shows enhanced activity toward the ORR compared to its counterparts with carboxyl-group or the pristine carbon. For the first time, as known, the CoO_x/C composite is used as the cathodic catalyst for the Zn-air battery, and the peak power density reaches up to 100–123 mW cm^{-2}, demonstrating the promising practical application in Zn-air battery. The enhanced ORR activity of the CoO_x/C—N composite is probably related with the higher content of CoO in the composite surface induced by the amide group over carbon surface.

Crown Copyright © 2013 Published by Elsevier B.V. All rights reserved.

1. Introduction

Oxygen reduction reaction (ORR) is of great importance for electrochemical energy conversion and storage devices such as fuel cells, metal–air batteries [1,2]. It is known that ORR involving multi-steps of electron transfer process is kinetically sluggish. Up to now, Pt and its alloys remain the most efficient ORR catalysts in both alkaline and acid media [3,4]. However, the high cost and scarcity of Pt limit its broad use practically. Exploring alternative catalytic materials becomes an urgent task presently.

Owe to the faster kinetics of ORR in alkaline media and the improved materials stability afforded by the use of alkaline electrolyte [5,6], non noble metal materials such as metal macrocycles, metal oxides including spinels, and perovskites, have been extensively investigated [7–13]. Especially, nitrogen-doped carbon materials have attracted great attention due to their promising activity toward ORR [14–17]. For the N-doped carbon, despite the ongoing debates on the catalytically active center, the type and content of nitrogen incorporated into carbon matrix is deemed to be crucial for the ORR [18]. Nitrogen, except for being doped in carbon matrix, however, sometimes appears as N-containing functional groups over carbon surface. Up to now, the role played by the functional groups over carbon surface is mostly addressed to anchor the active phase aiming at improving the stability or metal dispersion [19–21]. Whether N-containing functional groups over carbon surface influences the ORR activity is rarely investigated.

In this work, we report a facile method to modify the carbon surface with amide groups. The synthesis process is presented in Fig. 1. After loaded with cobalt oxide nanoparticles, the amide-group decorated carbon, compared to the pristine carbon and the carboxyl-group decorated carbon, shows superior activity toward the ORR. For the first time, as we known, the CoO_x/C—N composite is used as the cathode catalyst of a Zn-air battery [22], which shows much better performance compared to the commonly used MnO_2 catalyst.

2. Experimental

2.1. Grafting functional groups over carbon surface

Ten gram of carbon black (Vulcan XC-72 from Cabot, denoted as XC) was dispersed in 700 mL of 5 mol L^{-1} aqueous nitric acid in a round bottom flask. The mixture was refluxed at 110 °C for 6 h, then filtered, washed with copious of de-ionized water. After dried at 120 °C in an oven for 12 h, black powder was obtained and denoted as XC—O.

* Corresponding authors. Tel.: +86 0411 84379063; fax: +86 0411 84379063.
  E-mail addresses: sunshine@dicp.ac.cn (L. Jiang), gqsun@dicp.ac.cn (G. Sun).
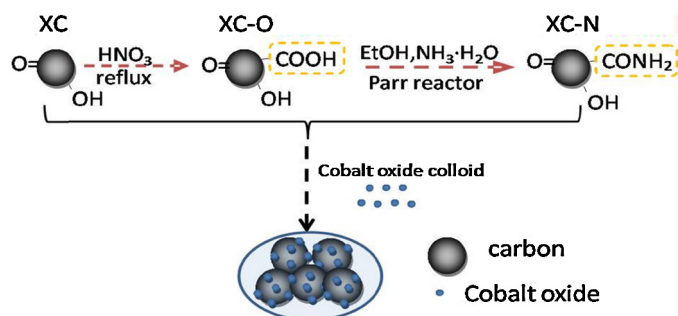
Fig. 1. Scheme of the modification of carbon surface with different functional groups and the deposition of cobalt oxide nanoparticles. XC, XC—O and XC—N stand for the pristine, carboxyl-group modified and amide-group modified Vulcan XC 72, respectively.

Five-hundred milligram of XC—O was further dispersed in 200 mL of ethanol plus 1 mL 25 wt.% ammonia for solvothermal treatment, i.e., 160 °C for 3 h. After that, removed the solvent by rotating evaporation and dried the sample at 80 °C in an oven overnight. The obtained carbon was denoted as XC—N.

The multiwall carbon nanotubes (MWCNT) and Black Pearls 2000 (BP) were modified following the same procedure and denoted as MWCNT-N and BP-N, respectively.

2.2. Synthesis of cobalt oxide nanoparticles and composite catalysts

The CoO_x colloid was synthesized by a modified solvent reflux method as described by Dong et al. [23] under ambient atmosphere. Briefly, 0.5 g of tetra-hydrated cobalt acetate ($Co(CH_3COO)_2 \cdot 4H_2O$) was dissolved in 25 mL of ethanol (EtOH), then 2.5 mL of 25 wt.% ammonia was added to the above solution under electromagnetic stirring. The mixture was stirred in air for about 15 min followed by refluxing at 100 °C for 3.5 h in a flask of 250 mL. Eighty milligram of carbon black powder, i.e., XC, XC—O, or XC—N was dispersed in 25 mL EtOH to form a uniform ink. The calculated amount of CoO_x colloid was added into the ink under electromagnetic stirring. The mixture was stirred for 6 h at room temperature, and dried at 80 °C in an oven overnight after evaporating the solvent. The obtained samples were denoted as: CoO_x/XC, CoO_x/XC—O, and CoO_x/XC—N. The cobalt loading in the three samples is kept the same as 5.9% (a theoretical value referred to the ratio in mass of cobalt to the total amount of cobalt and carbon).

2.3. Physical characterizations

The characterization on the carbon blacks, e.g., the specific surface areas and pore structure, was carried out using a QuadraSorb Station 3. Adsorption isotherms were obtained via N_2 adsorption at 77 K. BET surface area and pore-width were calculated by applying Brunauer–Emmett–Teller (BET) equation. Transmission electron microscopy (TEM) measurements were carried out using a JEM-2011EM microscope operated at 120 kV. Fourier transform infrared (FTIR) transmission spectra for the carbon blacks were recorded on a Thermo Fisher Nicolet 6700 FTIR spectrometer equipped with an MCTA detector by no. of scans of 128 with a resolution of 8 cm^{-1}. The catalyst powder mixed with KBr was pressed into a disk for FTIR measurements. X-ray photoelectron spectroscope (XPS, ESCALAB 250Xi) with X-ray sources of Al Kα was used to investigate the functional groups of carbon surfaces and the surface composition of the catalysts.

2.4. Electrochemical measurements

The electrochemical setup comprised of a computer controlled bipotentiostat, a radiometer speed control unit from Pine Instrument Company (MSRX Speed control), and a rotating disk electrode radiometer. The rotating disk electrode (RDE) is 5.0 mm in diameter. The electrochemical experiments were carried out with a conventional three-electrode cell. A Pt wire counter electrode and a Hg/HgO reference electrode in a 0.1 M NaOH solution purged with N_2 or O_2 at room temperature were used. All potentials initially measured vs. the Hg/HgO electrode were converted to values vs. RHE after calibration ($E_{vs. RHE}/V = E_{vs. Hg/HgO}/V + 0.926\,V$).

The catalyst ink was prepared as following: 5 mg of catalyst was dispersed in 2 mL ethanol and 30 μL Nafion (5 wt.% Dupont, USA). After ultrasonically blending for 15 min, 20 μL of the ink was pipetted on the glass carbon disk. The electrode was dried under a smooth flow of N_2.

2.5. Preparation of Zn-air single cell

The catalytic performance of the CoO_x/C as cathode electrocatalysts for air electrode of Zn-air cells was evaluated in a single cell of active geometric area of 32 cm^2. The air electrode was comprised of a Ni foam as both supports and a current collector, a gas diffusion layer, and a catalyst layer. The gas diffusion layer (GDL) was prepared by casting acetylene black with poly-tetrafluoroethylene (PTFE) (60 wt.% PTFE emulsion in water, Sigma–Aldrich) as bonders on one side of a Ni foam. The catalyst layer was prepared by casting a mixture of activated carbon (Sinopharm, Shanghai), acetylene black, catalysts and PTFE with a fixed ratio on the other side of the Ni foam. A Teflon film was laminated over the GDL to minimize electrolyte leakage and moisture diffusion. To enhance the contact degree of different components, the air electrode was finally pressed at a pressure of 18 MPa at room temperature for 1 min.

The Zn-air single cell was fabricated with a zinc plate as the anode and CoO_x/C electrode as the cathode. KOH aqueous solution (7 mol L^{-1}) is filled in the gap between anode and cathode as the electrolyte. Polarization curves were recorded at room temperature by employing a multichannel potentiostat (NEWARE Electronic Company, Shenzhen).

3. Results and discussion

3.1. Physical characterization of carbon supports

To identify the changes of surface functional groups on the Vulcan XC-72 under different treatments, Fourier transform infrared spectroscopy (FTIR) spectra of the carbon samples were collected in Fig. 2. For the three carbon samples, the common peaks centered at around 3400 cm^{-1} and 1583 cm^{-1} should be assigned to the O—H stretching vibration and the C=O stretching vibration [24], respectively. Compared to the spectra for XC, a distinct new peak at 1740 cm^{-1} appears for XC—O, which is assigned to the stretching vibration of C=O in O—C=O, indicating the treatment of XC with nitric acid grafts carboxyl groups successfully over carbon surface. In contrast, this peak becomes indistinct for XC—N. It is deduced that O—C=O groups over XC—O surface probably react with ammonia to generate amide groups (CO—NH$_2$), since the conjugated effect caused by the N adjacent to C=O in amide group (CO—NH$_2$) is well known surpassing the inductive effect, thus the characteristics of C=O in amide group is weakened compared with that in the carboxyl group [25]. More discussion will be presented later combining with the XPS analysis. A distinct difference between XC—O and XC—N is the occurrence of the new peaks at around 2923 and 2853 cm^{-1} for the latter, which is assigned to the symmetric
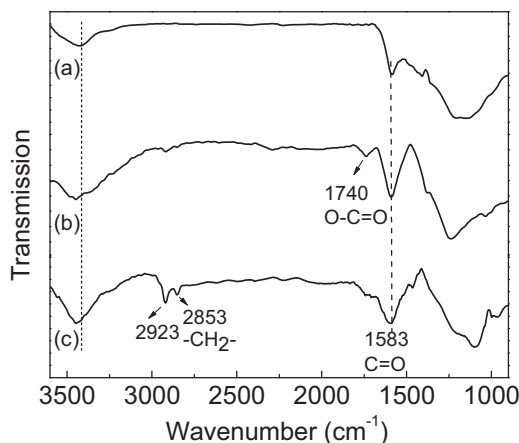
Fig. 2. FTIR spectra of XC (a), XC—O (b) and XC—N (c).

and asymmetric stretching vibrations of C—H in aliphatic CH, CH_2, and CH_3 groups [26], possibly resulting from the adsorbed ethanol molecules on surface traced back to the synthesis process. The failure to observe any peaks assigned to the amide groups might be due to the overlapping of the stretching vibration of O—H and some vibration of N—H at near $3400\,cm^{-1}$ [27].

We further characterize the surface composition and structural properties of the carbon supports comprehensively by XPS and N_2 adsorption techniques. The XPS survey spectra for carbon samples were shown in Fig. 3. The elemental composition in surface and the surface area as well as the textural information are summarized in Table 1. The elemental composition in surface of the carbon supports, determined by XPS, shows that O and N content for XC—O increase significantly while C and S content decrease compared to that for XC. Experienced further solvothermal treatment in the solvent of ammonia-containing ethanol, the O content for XC—N decreases by 0.59% but the N content enhances by 0.75% compared with XC—O, meanwhile, the content of carbon in surface of XC—N varies a little. It seems that the increase in N content is at the sacrifice of O and originates from the nitrogen in ammonia. The XPS
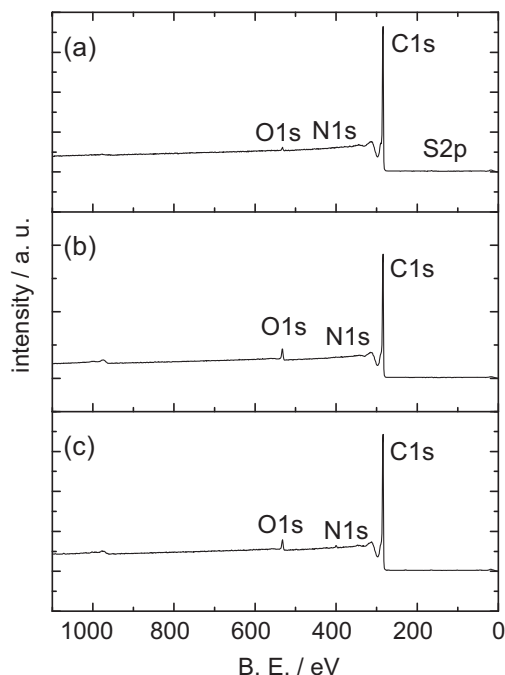

Fig. 3. XPS survey spectra of XC (a), XC—O (b) and XC—N (c).

results (decrease in O content and increase in N content), combining with the fact that the peak for C=O in O—C=O for XC—N becomes weakened as characterized by the FTIR spectra, support our deduction that the amide groups are attached on carbon surface by a reaction between carboxyl groups with ammonia. N_2-adsorption experiments show clearly that the treatment of carbon in nitric acid enlarges the average pore size of XC from 5.9 to 7.5 nm, resulting in a decrease in BET surface area by 11% due to the lessened contribution from the micropores. The subsequent solvothermal treatment further enlarges the average pore size to 8.3 nm, thus the BET surface area decreases further by 42% compared to that for the pristine XC.

Curve fitting of XPS O 1s spectra of carbon supports are shown in Fig. 4a–c which is deconvoluted into two peaks. The peak locating at near 532.0 eV might come from three contributions, i.e., the oxygen in quinine type carbonyl groups, carbonyl oxygen in anhydrides/lactones and oxygen in phenolic/ether groups [28,29]. The peak centered at around 533.0 eV is assigned to oxygen in carboxylic and the ether oxygen in lactones and anhydrides [28,29]. For XC and XC—O, the integrated area for the peak at 532.0 eV is equal to that for the peak at 533.0 eV, while for XC—N the integrated area for the peak at 533.2 eV is relatively lower than that for the peak at 531.7 eV, indicating a decrease in the content of carboxyl groups over XC—N surface. The XPS N 1s spectra of carbon supports are shown in Fig. 4d–f. Unlike the asymmetric peak of N 1s for N-doped carbon extensively reported in literature [30–32], in which several types of N, e.g., pyridinic, pyrrolic, pyridonic and quaternary N, present simultaneously, the XPS N 1s peak obtained in this work is rather symmetric, suggesting a different N type from the above listed. Generally, the N 1s spectra for XC—O and XC—N are deconvoluted into two peaks, centered at around 400.0 and 405.0 eV, respectively. In addition, the nitrogen signal for XC is too weak to be deconvoluted. Specifically, the N 1s peaks for XC—O showed two components at 400.8 eV and 405.7 eV, ascribing to the nitrogen in N—O and N=O, respectively. For XC—N, except the peak component at 405.0 eV assigned to the nitrogen in N=O, another peak component centered at 399.7 eV is observed which is assigned to the nitrogen in N—H groups. The disappearance of N—O in XC—N indicates that a fraction of the N—H groups might be from reduction of N—O under the reaction condition, although most of the N—H groups existing in the amide groups are likely to be introduced by a reaction between ammonia and carboxyl group on carbon surface, supported by the fact of decrease in amount of the carboxyl groups on XC—N surface characterized by both XPS and FTIR.

3.2. Physical characterization of CoO_x/C composites

Cobalt oxide nanoparticles were supported on XC, XC—O, and XC—N, denoted as CoO_x/XC, CoO_x/XC—O and CoO_x/XC—N, respectively. The bright-field and dark-field TEM images of the three composites are shown in Fig. 5. Cobalt oxide nanoparticles with average particle size of 2 nm are distributed uniformly on carbon supports for the three composites.

To further investigate the surface chemical state of the CoO_x in CoO_x/C composites, XPS measurements were carried out. The XPS surveys and high revolution XPS spectra of Co 2p of CoO_x/XC, CoO_x/XC—O and CoO_x/XC—N are shown in Fig. 6a and b. The surface atomic content of Co in the three samples is 3.75%, 3.94% and 3.67%, which is almost identical. As we can see in Fig. 6b, the common feature for the three samples is that two broad main peaks, Co $2p_{1/2}$ and Co $2p_{3/2}$, are separated by a spin-orbit splitting of 15.6 eV together with two strong associated satellites located at the high binding energy side of the main peaks (denoted as "S"). The strong satellites are the typical characteristics of cobalt in CoO [33]. The binding energy of Co $2p_{3/2}$ locates at about 780.7 eV which is in between of Co $2p_{3/2}$ in CoO (781.3–782.2 eV) and Co $2p_{3/2}$ in

Table 1
Summary of surface and structural information of carbons.

Sample	S_{BET} (m^2 g^{-1})	Micropore area (m^2 g^{-1})	Average pore size (nm)	Element content (at.%)[a]			
				C	O	N	S
XC	244	99	5.9	99.01	0.73	0.05	0.21
XC—O	217	83	7.5	95.97	3.72	0.16	0.15
XC—N	142	16	8.3	95.81	3.13	0.91	0.15

[a] Data from XPS analysis.
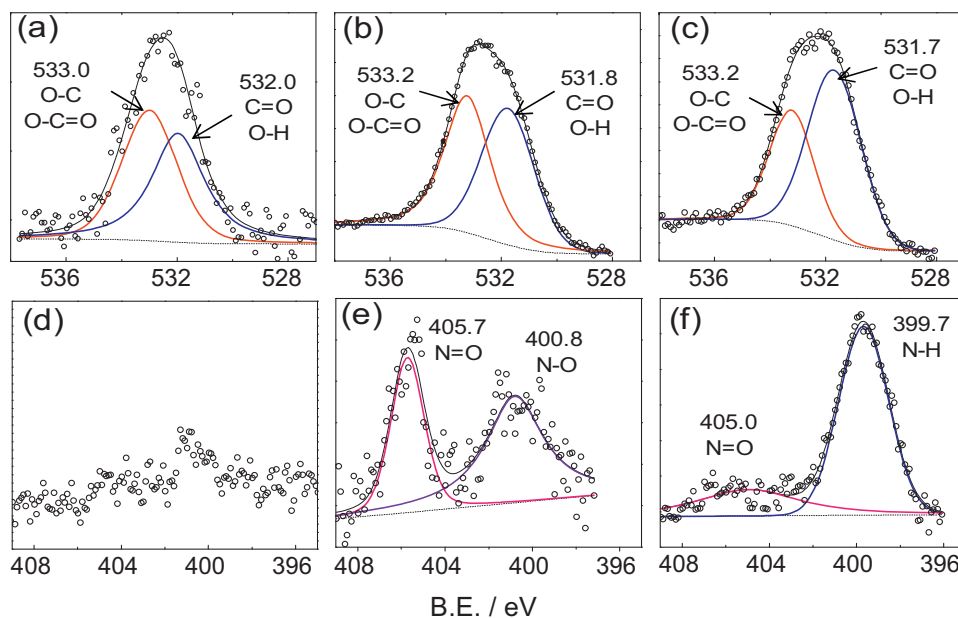
Fig. 4. XPS O 1s spectra of XC (a), XC—O (b), XC—N (c) and N 1s spectra of XC (d), XC—O (e), XC—N (f).

Co_3O_4 (779.6–780.6 eV) [33,34]. This suggests that cobalt oxide in the three composites consist of both CoO and Co_3O_4 in surface. To analyze the comparative percentage of CoO and Co_3O_4 in surface, the main peak of Co 2p$_{3/2}$ is deconvoluted into two peaks located at around 781.5 eV and 780.2 eV corresponding to CoO and Co_3O_4, respectively. By integrating the areas of each peak, the ratio of CoO to Co_3O_4 for CoO$_x$/XC, CoO$_x$/XC—O and CoO$_x$/XC—N is calculated to be 0.8:1, 1.9:1 and 2.0:1, respectively. It gives clues that the
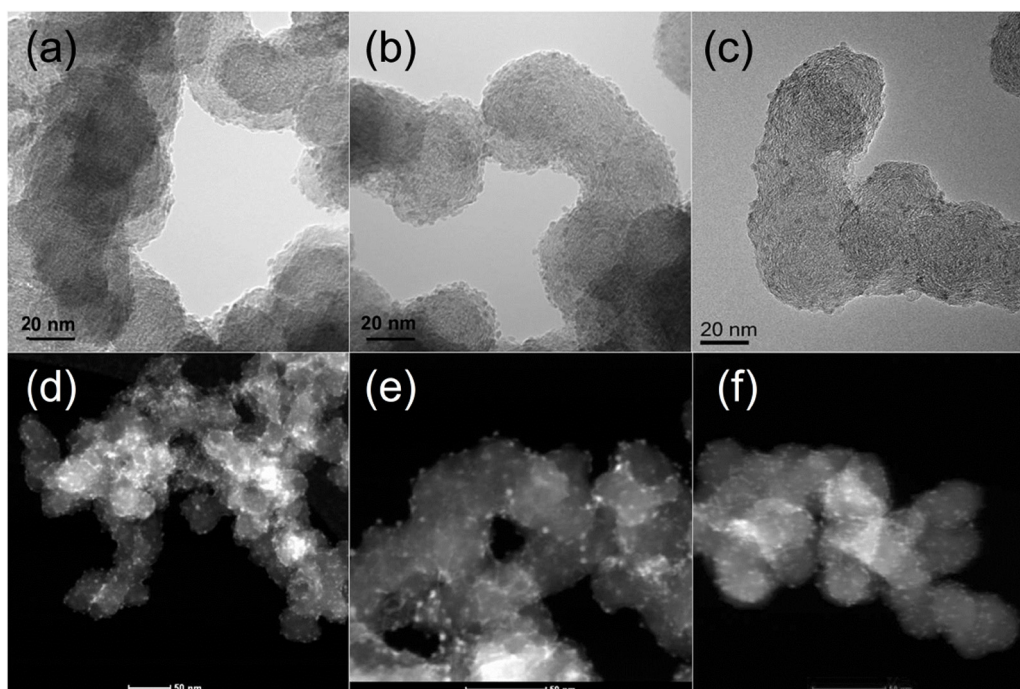
Fig. 5. Bright field TEM images of CoO$_x$/XC (a), CoO$_x$/XC—O (b) and CoO$_x$/XC—N (c), and dark field TEM images of CoO$_x$/XC (d), CoO$_x$/XC—O (e) and CoO$_x$/XC—N (f).
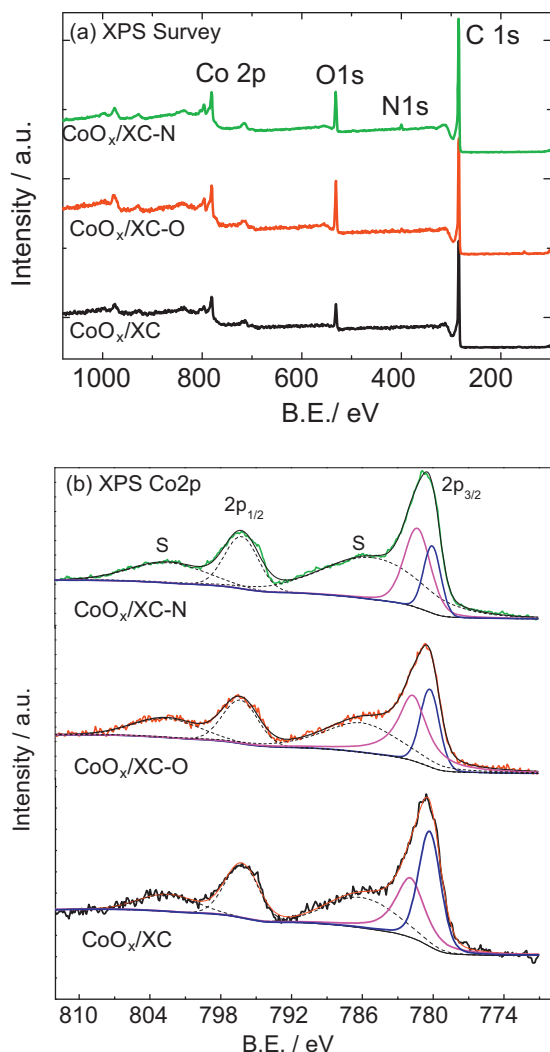
Fig. 6. XPS survey spectra (a) and Co 2p spectra (b) of CoO_x/XC, CoO_x/XC—O and CoO_x/XC—N.

Fig. 7. ORR polarization curves over CoO_x/XC, CoO_x/XC—O and CoO_x/XC—N (a). The ORR kinetic current density taken at the potential of 0.8 V over CoO_x/XC, CoO_x/XC—O and CoO_x/XC—N (b). Scan rate: $10\,mV\,s^{-1}$; rotating rate: 1600 rpm.

chemical modification of carbon surface might affect the surface composition of the supported CoO_x nanoparticles. Similar effect was also reported by Gorlin et al. on the MnO_x system, in which different surface compositions of MnO_x were observed due to different substrates [35]. We will throw a light on the origin of the substrate induced surface composition later combining with the DFT calculation.

3.3. Activity of CoO_x/C toward ORR

The ORR polarization curves over the three composites, measured in an O_2-saturated 0.1 M NaOH solution, are plotted in Fig. 7a. The onset potential for the ORR over the three catalysts is nearly the same at 0.86 V vs. RHE, while the ORR current density for the CoO_x/XC—N in the kinetic and diffusion mixed controlled region is enhanced. The ORR activity, reflected by the ORR half-wave potential, follows the trend of $CoO_x/XC < CoO_x/XC$—O $< CoO_x/XC$—N. The ORR kinetic current density for the three composites at the potential of 0.8 V is calculated by Koutecky–Levich equation as below and shown in Fig. 7b:

$$\frac{1}{i} = \frac{1}{i_L} + \frac{1}{i_K} = \frac{1}{B\omega^{1/2}} + \frac{1}{i_K}$$
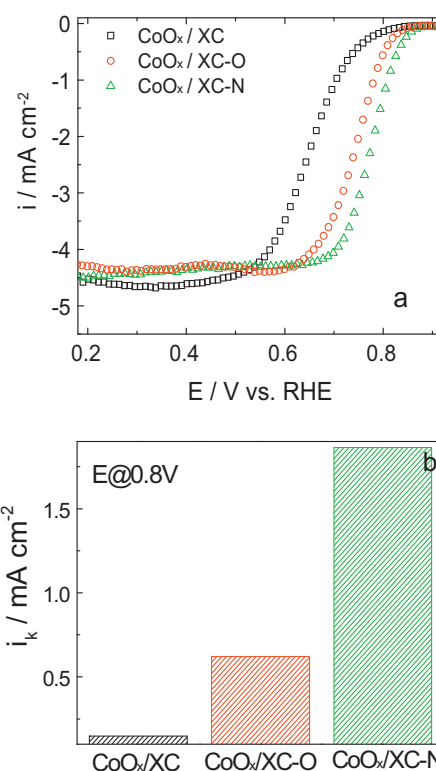
$$B = 0.62nFc_0 D_0^{2/3}\nu^{-1/6}$$

where i is the measured current density, i_K and i_L are the kinetic and diffusion limiting current density, ω is the angular velocity, n is the transferred electron number, F is the Faraday constant, c_0 is the bulk concentration of O_2, ν is the viscosity of the electrolyte. It can be seen from Fig. 7b that the ORR kinetic current density at 0.8 V for the CoO_x/XC—N is twelve folds and three folds of that for the CoO_x/XC and the CoO_x/XC—O, respectively. The electron transfer number for the ORR over the CoO_x/XC—N, calculated by Koutecky–Levich equation based on the ORR polarization curves at different rotating rates (Fig. 8), is around 3.7, suggesting that the composite material favors an overall $4e^-$ pathway toward ORR.

To expel the influence from carbon supports on the activity, we also tested the background CVs and ORR polarization curves over the carbons (Fig. 9). The ORR onset potential for the three carbons is similar, while the half-wave potential for XC—O is the most positive and that for XC the most negative, indicating XC—O is most active among the three carbons. The ORR activity for XC, XC—O and XC—N is in the same trend with that of their electrical double layer capacity. As we know, the electrical double layer capacity of carbon is related tightly with both surface functional groups and surface area (related with pore size), i.e., the more the surface functional groups and the larger the surface area, the higher the double layer capacity. In the case of XC, XC—O and XC—N, the electrical double layer capacity is in the trend of XC—O > XC—N > XC which follows the trend of surface oxygen containing group content in the carbons, but not the trend of the surface area, suggesting the surface functional groups contribute more to the electrical double layer capacity than the surface area. This result highly agrees with previous reports that functional groups on carbon surface, especially oxygen containing groups, like quinine, acts as the active sites for the ORR [36,37]. Comparatively, the surface area and pore size of
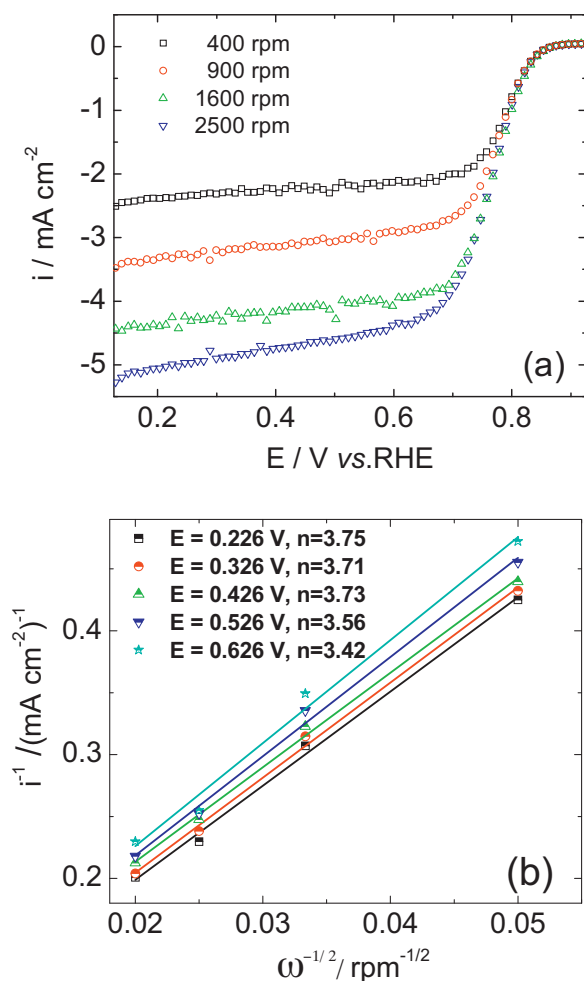
Fig. 8. ORR polarization curves on CoO_x/XC—N at different rotating rates (a) and the corresponding Koutecky–Levich plots at different potentials (b). Scan rate: $10\,mV\,s^{-1}$.
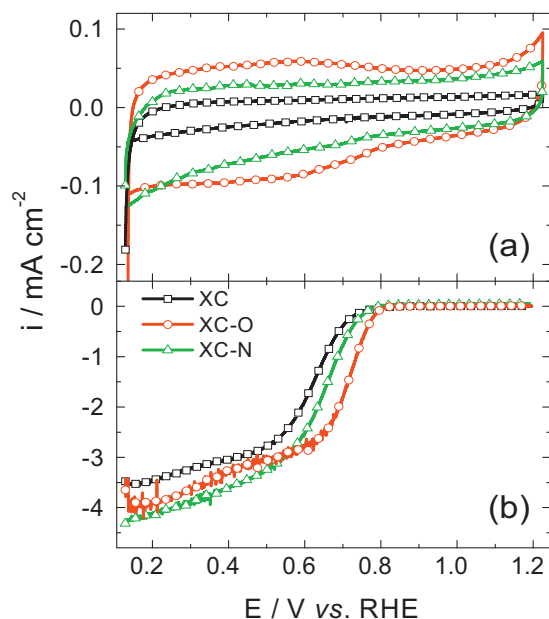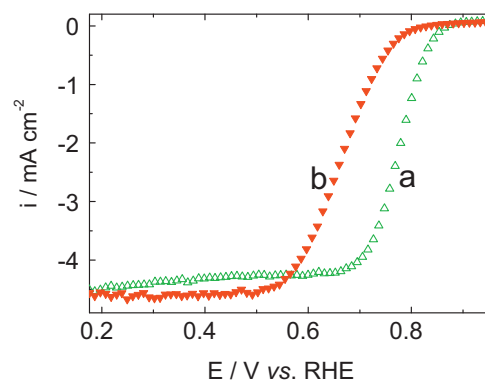

Fig. 10. ORR polarization curves for the CoO_x/XC—N (a) and CoO_x/XC-ST (b). Catalyst loading: $255\,\mu g\,cm^{-2}$; scan rate: $10\,mV\,s^{-1}$; rotating rate: $1600\,rpm$.

carbons seem to have little influence on the ORR activity. Furthermore, the low ORR activity of the XC—N, compared to the XC—O, provides evidence again that the nitrogen is not doped into carbon matrix, but in forms of nitrogen-containing functional groups over carbon surface. Otherwise, the XC—N, if N were doped in carbon matrix in form of pyridinic or pyrrole-type nitrogen, would present rather high activity toward the ORR as reported extensively. Although carbon with non-doped nitrogen did not show significant improvement on ORR activity, once loaded with cobalt oxide, the composite CoO_x/XC—N show the best activity among the three catalysts as discussed above.

Considering that the average particle size of the CoO_x in all composites is identical and the distribution of the CoO_x particles on carbon surface is similarly uniform, the particle size effect could be excluded. Thus, the special high activity for the CoO_x/XC—N might be related with the surface CoO_x composition which is tuned by the unique carbon surface. To investigate whether the amide-groups on carbon surface is absolutely necessary for the high ORR activity, we have to exclude the influence from the carbon surface area, so additional two carbon supports, i.e., XC—N and its counterpart with comparable surface area and textural construction but without amide-groups on surface are compared. To this end, we treated the XC following the same procedure as XC—N but without ammonia adding during the solvothermal treatment. As expected, the obtained carbon, denoted as XC-ST, possesses a similar BET surface area ($110\,m^2\,g^{-1}$) and average pore size ($7.7\,nm$) as those for XC—N with BET surface area of $142\,m^2\,g^{-1}$ and average pore size of $8.3\,nm$. After loading CoO_x NPs, the CoO_x/XC-ST composite shows much poor activity for ORR compared to the CoO_x/XC—N as expected (Fig. 10). This confirms again that the good activity for the CoO_x/XC—N does benefit from the unique nitrogen-containing groups on carbon surface and consequently induced higher content of CoO.

We further extend the amide-group modified carbon support to multi-wall nanotubes (MWCNT, $S_{BET} = 200\,m^2\,g^{-1}$) and Black Pearls 2000 (BP, $S_{BET} = 1562\,m^2\,g^{-1}$) by the same modification procedure. The ORR polarization curves over cobalt oxides supported on different types of carbon supports with amide groups are presented in Fig. 11. After decorated with amide-groups, the half-wave potential ($E_{1/2}$) of ORR curves for all CoO_x/C—N composites shift positively, indicating that the beneficial effect by the amide-groups on the ORR is a universal phenomenon, not just limited to Vulcan XC 72 carbon black. A notable difference for the ORR over the CoO_x/MWCNT composites, compared to that over the CoO_x/XC and CoO_x/BP composites, is the i_{lim} of ORR over the CoO_x/MWCNT is only half of that over the CoO_x/MWCNT-N even though both composites are of the identical thickness of catalyst layer, which confirms strongly that amide-group grafting on carbon surface did

Fig. 9. Base CVs (a) and ORR polarization curves (b) for XC, XC—O and XC—N. Carbon loading: $196\,\mu g\,cm^{-2}$; scan rate: $10\,mV\,s^{-1}$; rotating rate: $1600\,rpm$.
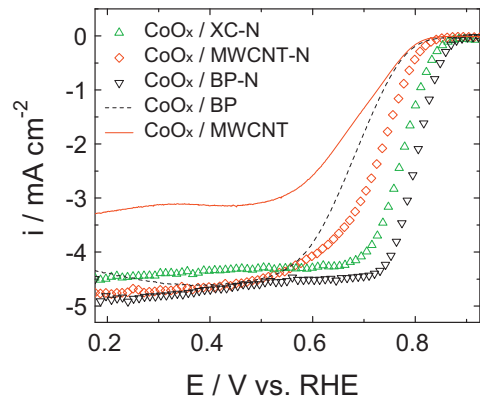
Fig. 11. Comparison of ORR polarization curves over CoO_x/XC—N, CoO_x/MWCNT-N, CoO_x/BP-N and CoO_x on pristine MWCNT and BP. Catalyst loading: 255 μg_{cat} cm^{-2}; scan rate: 10 mV s^{-1}; rotating rate: 1600 rpm.

Fig. 12. Polarization curves of Zn-air cells with different air electrodes: CoO_x/XC, CoO_x/XC—O and CoO_x/XC—N. Home-made MnO_x/XC and Pt/XC represented as comparisons. The insert is the enlargement of the selected activation polarization controlled region.

enhance intrinsically the ORR activity of the composite. In contrast, the comparable i_{lim} over both CoO_x/XC and CoO_x/BP composites with/without amide-group modification testifies again the reaction coupling effect existing between CoO_x and carbon at a thicker catalyst layer as supposed in our previous work [38].

3.4. Zn-air single cell performance

Five single zinc air cells with CoO_x/XC, CoO_x/XC—O, CoO_x/XC—N, Pt/XC and MnO_2/XC as the respective cathode catalyst were fabricated and the discharging I–V curves are presented in Fig. 12 for comparison. It can be seen that the open circuit voltage of the single cell with CoO_x/XC—N as the cathode catalyst is 1.464 V, which is slightly higher than that with CoO_x/XC—O (1.458 V) or CoO_x/XC (1.457 V), but all are higher than that with Pt/XC or MnO_2/XC as the cathode catalyst (1.418 V and 1.373 V respectively). At the low current density (0–10 mA cm^{-2}), i.e.,
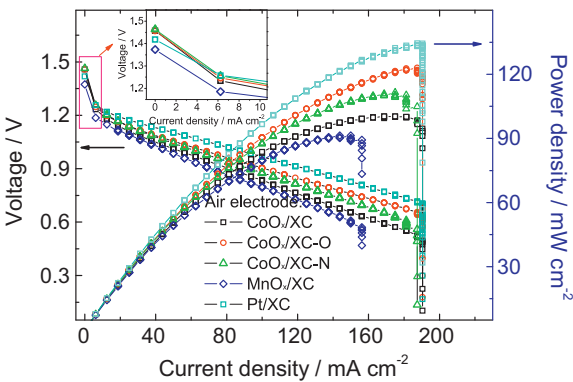
the activation polarization region, the cell voltage follows the trend of Pt/XC ≈ CoO_x/XC—N > CoO_x/XC—O > CoO_x/XC > MnO_2/XC, which follows the trend of the activity toward the ORR tested in the half cells, demonstrating that CoO_x/XC—N composite have superior intrinsic activity toward ORR over its counterparts, whether CoO_x/XC—O or CoO_x/XC. With the discharging current density further increasing, the polarization enters the ohmic polarization and then mass transport polarization regions. The peak power density of the cell follows the sequence of Pt/XC (~136 mW cm^{-2}) > CoO_x/XC—O(~123 mW cm^{-2}) > CoO_x/XC—N (~110 mW cm^{-2}) > CoO_x/XC (~100 mW cm^{-2}) > MnO_2/XC (~90 mW cm^{-2}). Such a trend does not follow the same order as that in the activation polarization region, which is explainable considering the cell performance is governed not only by the activity of electrocatalysts but also by both ohmic resistance and the mass transport in the electrodes in the ohmic polarization region and the mass transport polarization region. However, it is not the topic

Table 2
Summary of the DFT calculation results: the most stable geometric structures of the O—Co—C—CONH$_2$ and O—Co—C—COOH clusters, the corresponding Mulliken atomic charges, energy gap (ΔE_{L-H}) of the lowest unoccupied orbital (LOMO) and highest occupied orbital (HOMO).

Cluster	Geometric structure	Mulliken atomic charges			ΔE_{L-H} (Hartree)
O—Co—C—CONH$_2$		1	C	0.33676	0.10985
		2	O	−0.33530	
		3	C	−0.59425	
		4	N	−0.43854	
		5	H	0.23295	
		6	H	0.23798	
		7	Co	1.17296	
		8	O	−0.61255	
O—Co—C—COOH		1	C	0.31787	0.11042
		2	O	−0.31450	
		3	C	−0.55157	
		4	Co	1.19901	
		5	O	−0.59620	
		6	O	−0.31126	
		7	H	0.25666	

of this paper. Detailed investigation on the mass transfer in the air electrode will be discussed in another paper.

3.5. Origin of reactivity of CoO$_x$/C toward ORR

As discussed above, carbon with different surface functional groups is able to influence the chemical state of the cobalt oxides supported on carbon surface, and thus the ORR activity. To discover the origin of the substrate-induced phase change of cobalt oxides and the reactivity of CoO$_x$/C toward ORR, density function theory (DFT) calculation was carried out by modeling CoO$_x$ interacts with the functionalized carbon supports. The CoO$_x$/XC—N and CoO$_x$/XC—O catalysts were simplified as cluster O—Co—C—CONH$_2$ and O—Co—C—COOH, respectively, based on the physical characterization information. The DFT calculation was performed at the B3LYP level [39,40] with the Gaussian 03 program [41]. The Los Alamos LANL2DZ effective core pseudopotential (ECP) [42,43] was adopted for the Co atom and a basis set of 6-311G** is used for C, H, N and O atoms. For the O—Co—C—CONH$_2$ and O—Co—C—COOH clusters, geometry optimization was performed with different geometries and spin states. The most stable geometries of O—Co—C—CONH$_2$ and O—Co—C—COOH clusters were further considered for analysis. The frequency calculations were also performed to verify that the frequencies of all the geometries were positive. The most stable geometries together with the corresponding Mulliken atomic charges and the energy gap between the highest occupied molecular orbital (HOMO) and the lowest unoccupied molecular orbital (LUMO) energies are listed in Table 2. The Mulliken atomic charge of Co in O—Co—C—CONH$_2$ cluster is less than that in O—Co—C—COOH cluster, consistent well with the XPS analysis that higher CoO content in the surface of CoO$_x$/XC—N than that of CoO$_x$/XC—O, which is reasonable since amide group is more prone to donate electron than carboxyl group. This explains intrinsically the higher CoO content in CoO$_x$/C—N composite. Recently, Xiao et al. studied the ORR over Co$_3$O$_4$ exposing different crystalline surface and proposed the surface Co (II) is responsible for the high ORR activity [44]. He et al. also reported a high active CoO hybrid graphene composite toward ORR [45]. Accordingly, Co (II) is expected to be involved in the active site for ORR. In our case, the content of CoO in surface follows the trend of CoO$_x$/XC—N > CoO$_x$/XC—O > CoO$_x$/XC. Thus, the higher content of CoO in surface of the CoO$_x$/XC—N composite is supposed to be responsible for the higher ORR activity. Theoretically, the chemical reactivity of the cluster is often correlated with the energy gap between HOMO and LUMO according to the frontier orbital theory. A small HOMO–LUMO gap implies low kinetic stability and high chemical reactivity, because it is energetically favorable to add electrons to a high-lying LUMO, to extract electrons from a low-lying HOMO, and so to form the activated complex of any potential reactions [46]. From Table 2, it can be seen that the energy gap between the HOMO and the LUMO for the O—Co—C—CONH$_2$ cluster is lower than that for the O—Co—C—COOH cluster, indicating a more active nature of the CoO$_x$/XC—N catalyst, thus leading to the observed enhanced ORR activity.

4. Summary

Carbon surface is decorated successfully by different functional groups, like carboxyl groups and amide groups via a facile solvothermal approach, on which cobalt oxide nanoparticles of around 2 nm are loaded to act as electrocatalysts for ORR. It is found the chemical state of the cobalt oxide over carbon surface is affected by the functional groups over carbon surface, i.e., amide groups induce more Co(II) on surface. Electrochemical test results show that the amide group functionalized composite (CoO$_x$/XC—N)

presents superior activity toward the ORR over its counterparts, i.e., cobalt oxide nanoparticles loaded on carbon with carboxyl-group (CoO$_x$/XC—O) or the pristine carbon (CoO$_x$/XC). As the cathode electrocatalyst for Zn-air batteries, the series of CoO$_x$/C composites display comparable performance to Pt/XC and better performance than the conventional MnO$_2$/XC electrode. Combined with the DFT calculation, the origin of the enhanced ORR activity of the CoO$_x$/XC—N is probably related with the higher content of CoO in surface and thus the smaller energy gap of HOMO–LUMO.

References

[1] U.A. Paulus, T.J. Schmidt, H.A. Gasteiger, R.J. Behm, J. Electroanal. Chem. 495 (2001) 134–145.
[2] F.Y. Cheng, J. Chen, Chem. Soc. Rev. 41 (2012) 2172–2192.
[3] N.M. Markovic, T.J. Schmidt, V. Stamenkovic, P.N. Ross, Fuel Cells 2 (2001) 105–116.
[4] Y.H. Bing, H.S. Liu, L. Zhang, D. Ghosh, J.J. Zhang, Chem. Soc. Rev. 39 (2010) 2184–2202.
[5] B.B. Blizanac, P.N. Ross, N.M. Markovic, Electrochim. Acta 52 (2007) 2264–2271.
[6] J.S. Spendelow, A. Wieckowski, Phys. Chem. Chem. Phys. 9 (2007) 2654–2675.
[7] J. Suntivich, H.A. Gasteiger, N. Yabuuchi, H. Nakanishi, J.B. Goodenough, S.H. Yang, Nat. Chem. 3 (2011) 546–551.
[8] F.Y. Chen, J. Shen, B. Peng, Y.D. Pan, Z.L. Tao, J. Chen, Nat. Chem. 3 (2011) 79–84.
[9] Y.Y. Liang, Y.G. Li, H.L. Wang, J.G. Zhou, J. Wang, T. Regier, H.J. Dai, Nat. Mater. 10 (2011) 780–786.
[10] Q.W. Tang, L.H. Jiang, J. Qi, Q. Jiang, S.L. Wang, G.Q. Sun, Appl. Catal. B: Environ. 104 (2011) 337–345.
[11] M.D. Koninck, S.C. Poirier, B. Marsan, J. Electrochem. Soc. 154 (2007) A381–A388.
[12] M.D. Koninck, B. Marsan, Electrochim. Acta 53 (2008) 7012–7021.
[13] M. Hamdani, R.N. Singh, P. Chartier, Int. J. Electrochem. Sci. 5 (2010) 556–577.
[14] C.H. Choi, S.H. Park, S.I. Woo, Appl. Catal. B: Environ. 119 (2012) 123–131.
[15] L.F. Lai, J.R. Potts, D. Zhan, L. Wang, L. Wang, C.K. Poh, C. Tang, H. Gong, Z.X. Shen, J.Y. Lin, R.S. Ruoff, Energy Environ. Sci. 5 (2012) 7936–7942.
[16] D.H. Deng, X.L. Pan, L.A. Yu, Y. Cui, Y.P. Jiang, J. Qi, W.X. Li, Q.A. Fu, X.C. Ma, Q.K. Xue, G.Q. Sun, X.H. Bao, Chem. Mater. 23 (2011) 1188–1193.
[17] G. Liu, X.G. Li, P. Ganesan, B.N. Popov, Appl. Catal. B: Environ. 93 (2009) 156–165.
[18] G. Wu, K.L. More, C.M. Johnston, P. Zelenay, Science 332 (2011) 443–447.
[19] J. Kim, S.W. Lee, C. Carlton, Y. Shao-Horn, J. Phys. Chem. Lett. 2 (2011) 1332–1336.
[20] W.M. Chen, Q. Xin, G.Q. Sun, Q. Wang, Q. Mao, H.D. Su, J. Power Sources 180 (2008) 199–204.
[21] S.M.S. Kumar, J.S. Herrero, S. Irusata, K. Scott, J. Electronal. Chem. 647 (2010) 211–221.
[22] R.G. Cao, J.S. Lee, M.L. Liu, J. Cho, Adv. Energy Mater. 2 (2012) 816–829.
[23] Y.M. Dong, K. He, L. Yin, A.M. Zhang, Nanotechnology 18 (2007) 435602.
[24] S. Biniak, G. Szymanski, J. Siedlewski, A. Swiatkowski, Carbon 35 (1997) 1799–1810.
[25] S.F. Weng, Fourier Transform Infrared Spectrometer, first ed., Chemical Industry, Beijing, 2005, pp. 249–254.
[26] L.F. Lai, G.M. Huang, X.F. Wang, J. Wang, Carbon 48 (2010) 3145–3156.
[27] F. Jia, K.M. Thomas, Langmuir 16 (2000) 1114–1122.
[28] M.H.M.T. Assumpcao, R.F.B. De Souza, D.C. Rascio, J.C.M. Silva, M.L. Calegaro, I. Gaubeur, T.R.L. Paixao, P. Hammer, M.R.V. Lanza, M.C. Santos, Carbon 49 (2011) 2842–2851.
[29] D. Lennon, D.T. Lundie, S.D. Jackson, G.J. Kelly, S.F. Parker, Langmuir 18 (2002) 4667–4673.
[30] H.R. Byon, J. Suntivich, E.J. Crumlin, Y. Shao-Horn, Phys. Chem. Chem. Phys. 13 (2011) 2143721445.
[31] S. Kundu, T.C. Nagaiah, W. Xia, Y.M. Wang, S.V. Dommele, J.H. Bitter, M. Santa, G. Grundmeier, M. Bron, W. Schuhmann, M. Muhler, J. Phys. Chem. C 113 (2009) 14302–14310.
[32] H. Wang, R. Cote, G. Faubert, D. Guay, J.P. Dodelet, J. Phys. Chem. B 103 (1999) 2042–2049.
[33] V.M. Jimenez, J.P. Espinos, A.R. Gonzalez-Elipe, Surf. Interface Anal. 26 (1998) 62–71.
[34] Y. Okamoto, T. Adachi, K. Nagata, M. Odawara, T. Imanaka, Appl. Catal. 73 (1991) 249–265.
[35] Y. Gorlin, B. Lassalle-Kaiser, J.D. Benck, S. Gul, S.M. Webb, V.K. Yachandra, J. Yano, T.F. Jaramillo, J. Am. Chem. Soc. 135 (2013) 8525–8534.

[36] C.J. Song, J.J. Zhang, in: J.J. Zhang (Ed.), PEM Fuel Cell Electrocatalysts and Catalyst Layers: Fundamentals and Applications, Springer, New York, 2008, pp. 102–110.
[37] M.S. Hossain, D. Tryk, E. Yeager, Electrochim. Acta 34 (1989) 1733–1737.
[38] J. Liu, L.H. Jiang, Q.W. Tang, B.S. Zhang, D.S. Su, S.L. Wang, G.Q. Sun, ChemSusChem 5 (2012) 2315–2318.
[39] A.D. Becke, J. Chem. Phys. 98 (1993) 5648–5652.
[40] C. Lee, W. Yang, R.G. Parr, Phys. Rev. B 37 (1988) 785–789.
[41] M.J. Frisch, G.W. Trucks, H.B. Schlegel, G.E. Scuseria, M.A. Robb, J.R. Cheeseman, J.A. Montgomery Jr., T. Vreven, K.N. Kudin, J.C. Burant, J.M. Millam, S.S. Iyengar, J. Tomasi, V. Barone, B. Mennucci, M. Cossi, G. Scalmani, N. Rega, G.A. Petersson, H. Nakatsuji, M. Hada, M. Ehara, K. Toyota, R. Fukuda, J. Hasegawa, M. Ishida, T. Nakajima, Y. Honda, O. Kitao, H. Nakai, M. Klene, X. Li, J.E. Knox, H.P. Hratchian, J.B. Cross, C. Adamo, J. Jaramillo, R. Gomperts, R.E. Stratmann, O. Yazyev, A.J. Austin, R. Cammi, C. Pomelli, J.W. Ochterski, P.Y. Ayala, K. Morokuma, G.A. Voth, P. Salvador, J.J. Dannenberg, V.G. Zakrzewski, S. Dapprich, A.D. Daniels, M.C. Strain, O. Farkas, D.K. Malick, A.D. Rabuck, K. Raghavachari, J.B. Foresman, J.V. Ortiz, Q. Cui, A.G. Baboul, S. Clifford, J. Cioslowski, B.B. Stefanov, G. Liu, A. Liashenko, P. Piskorz, I. Komaromi, R.L. Martin, D.J. Fox, T. Keith, M.A. Al-Laham, C.Y. Peng, A. Nanayakkara, M. Challacombe, P.M.W. Gill, B. Johnson, W. Chen, M.W. Wong, C. Gonzalez, J.A. Pople, Gaussian 03, Revision A.1, Gaussian, Inc., Pittsburgh, PA, 2003.
[42] P.J. Hay, W.R. Wadt, J. Chem. Phys. 82 (1985) 270–283.
[43] P.J. Hay, W.R. Wadt, J. Chem. Phys. 82 (1985) 299–310.
[44] J.W. Xiao, Q. Kuang, S.H. Yang, F. Xiao, S. Wang, L. Guo, Sci. Rep. (2013), http://dx.doi.org/10.1038/srep02300.
[45] Q.G. He, Q. Li, S. Khene, X.M. Ren, F.E. Lopez-Suarez, D. Lozano-Castello, A. Bueno-Lopez, G. Wu, J. Phys. Chem. C 117 (2013) 8697–8707.
[46] L.P. Zhang, Z.H. Xia, J. Phys. Chem. C 115 (2011) 11170–11176.